

Second Virial Coefficient Measurements of Dilute Gold Nanocrystal Dispersions Using Small-Angle X-ray Scattering

Aaron E. Saunders and Brian A. Korgel*

Department of Chemical Engineering, Texas Materials Institute and Center for Nano- and Molecular Science and Technology, The University of Texas, Austin, Texas 78712-1062

Received: June 29, 2004

Small-angle X-ray scattering (SAXS) was used to study the size-dependent two-body solvent-mediated interparticle interactions between dodecanethiol-coated gold nanocrystals (2–6 nm in diameter) in dilute toluene dispersions. Using a modified Zimm analysis of concentration-dependent X-ray scattering data, the second virial coefficient B_2 was measured as a function of nanocrystal diameter and compared to theoretical predictions. The measured values of B_2 are more negative than those expected for hard spheres, indicating that interparticle attractions are significant in this system, even though the particles are dispersed in good solvents for the ligands. The data can be fit using a square well potential to model the pair interactions with nanocrystal size-dependent well depths ranging between 0.1 and 0.4 kT and a range of interaction of 30 Å. The interaction potentials between particles in the larger size range (i.e., >5 nm diameter) are close to those expected from a simple steric stabilization model accounting for the core–core van der Waals attraction modified by an osmotic repulsion between adsorbed chains. Smaller particles, however, exhibited significantly stronger attraction than expected from this simple model, which could possibly be due to decreased ligand surface coverage at the smaller nanocrystal sizes.

Introduction

Sterically stabilized colloidal semiconductor and metal nanocrystals, ranging from 2 to 10 nm in diameter, exhibit unique size-tunable properties and could prove important for a variety of new technologies, including catalysis, electronic and photonic devices, and biological sensors.^{1–4} A variety of nanocrystals can now be synthesized with reasonable size control by arrested precipitation—a process that utilizes organic ligands to stabilize the particle size and prevent flocculation.⁵ The ligands chemically passivate the nanocrystal surfaces and enable the particles to be dispersed in solvents. Dispersed particles can then be separated by size and shape through solvent/antisolvent techniques^{6,7} or dried into films by casting or spraying.⁵ Much interest has recently focused on understanding and controlling nanocrystal organization during the drying process, and it is now well-understood that the gross morphology and nanocrystal packing structure in dried films depend on the nanocrystal size distribution, deposition kinetics, and solvent-mediated interparticle interactions.^{7–19} Under conditions of *quasi-reversible* solvent evaporation, nanocrystals exhibit equilibrated colloidal phase behavior that is related to the solvent-mediated two-body interparticle interactions; for example, monodisperse nanocrystals experiencing strong repulsive interactions undergo a disorder–order phase transition at high volume fractions due to excluded-volume effects.^{12,13,20,21} In *nonequilibrium* systems, where solvent evaporation plays an influential role,^{14,18,19} the interparticle interactions are still central to the self-organization process as they influence the particle assembly dynamics relative to the solvent dynamics. In addition to affecting nanocrystal

self-assembly, the interparticle attractions also play a central role in size-selective precipitation^{6,7,22} and colloidal nanocrystal aging.

For nanometer-diameter nanocrystals, small-angle X-ray scattering (SAXS) provides a powerful analytical tool for measuring the particle size distribution, interparticle interactions, and collective structure. In SAXS, scattering arises from the difference in electron density between the nanocrystal core and the surrounding medium. The intensity of scattered radiation $I(q)$ can be expressed as a proportional relationship between a shape factor $P(qR)$ and structure factor $S(q)$: $I(q) \propto P(qR)S(q)$.^{7,20,23,24} The shape factor depends on the interference between X-rays scattered *within* an isolated particle, while the structure factor arises from the interference between X-rays scattered from multiple particles. $P(qR)$ relates to the size and shape of individual particles: for a solid homogeneous sphere, $P_0(qR) = [3(\sin(qR) - qR \cos(qR))/(qR)^3]^2$, where R is the radius of the metal core, q is the wave vector, $q = (4\pi/\lambda) \sin(\theta)$, related to λ , the photon wavelength ($\lambda(\text{Cu K}\alpha) = 1.54 \text{ Å}$), and 2θ is the scattering angle.^{20,23} Sample polydispersity is easily accounted for in SAXS measurements since the total scattered X-ray intensity from dispersions with noninteracting particles relates simply to the total number of scatterers, leading to a modified shape factor: $P(qR) \propto \int N(R)P_0(qR)R^6 dR$, where $N(R)$ is the nanocrystal size distribution.²³ In dilute dispersions with *noninteracting* particles,²⁵ $S(q) \approx 1$, such that the scattered intensity depends only on the shape factor, $I(q) \propto P(qR)$. In systems with *interacting* particles, $S(q) \neq 1$. In very concentrated systems, such as dried films, the interference between X-rays scattered from *multiple* particles dominates the scattering pattern. For example, scattering from superlattices gives rise to Bragg diffraction.²⁰ In dilute dispersions, the effect of multiparticle scattering between interacting particles is subtle. From Zimm's early analysis of dilute macromolecular dispersions,²⁶ the

* To whom correspondence should be addressed: Tel 512-471-5633; Fax 512-471-7060; e-mail korgel@mail.che.utexas.edu.

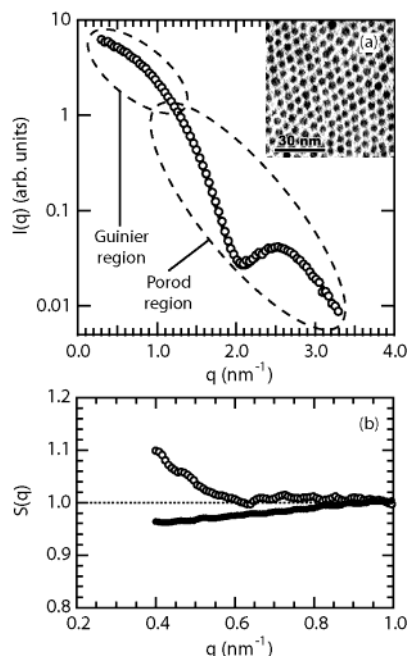


Figure 1. (a) SAXS data (○) and TEM image (inset) obtained from a toluene dispersion of 42 Å gold nanocrystals capped with dodecanethiol. The solid line represents the best fit of $P(qR)$ to the data using a Gaussian size distribution with an average radius of 21.4 Å and standard deviation of 2.3 Å (11%). The Guinier region at low q contains information about the electronic radius of gyration and particle interactions. At larger q , the location and intensity of the oscillations in the Porod region contain information about the shape and size distribution of nanocrystals in the dispersion. (b) Measured values of $S(q)$ at low q for dispersions of dodecanethiol-coated gold nanocrystals with core diameters of 30 (○) and 49 Å (●). Positive deviations from unity indicate attractive interactions while negative deviations indicate repulsive interactions.

structure factor results largely from two-particle scattering interference, and the mathematical form reflects the dependence on both interaction strength and solute concentration, such that $S(q,c) = 1 - \xi P(qR)$. Here the parameter ξ depends on the concentration of scatterers c , the osmotic second virial coefficient A_2 , and the weight-average molecular weight M_w : $\xi = 2A_2cM_w$.²⁷ It is then obvious from the form of $S(q,c)$ that the magnitude of the deviation from the shape factor due to pairwise interactions between particles will depend on the concentration of the dispersion. The osmotic second virial coefficient A_2 relates directly to the second virial coefficient obtained from statistical mechanics B_2 , which is an integral measure of the pair interaction potential $u(r)$ experienced by particles in solution:^{28,29}

$$B_2 = A_2 v_c \frac{M_w^2}{N_A} = -2\pi \int (e^{-u(r)/kT} - 1) r^2 dr \quad (1)$$

N_A is Avogadro's number, r is the center-to-center particle separation, and v_c is the ratio of the solvent and nanocrystal molar volumes.

In dilute dispersions, $\xi P(qR) \ll 1$, except at low q where this factor can become significant. As shown in Figure 1a, this region in the scattering curve is known as the Guinier region. Scattering at higher q —in the Porod region—is dominated by intraparticle scattering and is not affected by weak interparticle interactions. Both repulsive and attractive interparticle interactions can lead to deviations from $P(qR)$ at small q . Repulsive interparticle interactions give rise to $A_2 > 0$ and negative

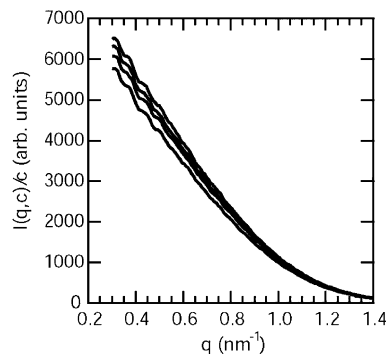


Figure 2. Scattered intensity in the Guinier region from dispersions of 53 Å dodecanethiol-coated gold nanocrystals in toluene at different mass concentrations. The intensities have been normalized by dividing by the concentration of each sample. The mass concentrations of the gold cores in the dispersions, from top to bottom, are 1.72, 2.02, 2.30, and 2.59 mg/mL. The repulsive interactions between particles results in decreased scattering at low q for more concentrated samples.

deviations from the scattering expected from noninteracting particles. $A_2 < 0$ when significant interparticle attraction occurs, which gives rise to positive deviations from the noninteracting particle scattering curves. For example, Figure 1b shows examples of both $S(q) > 1$ and $S(q) < 1$ measured for dodecanethiol-coated gold nanocrystals dispersed in toluene (~ 3 mg/mL) as a result of attractive and repulsive interactions, respectively, between particles in the dispersions. Figure 2 shows an example of how particle concentration affects the X-ray scattering intensity at low q for 53 Å diameter dodecanethiol-coated gold nanocrystals. For these particles, $S(q) < 1$ due to repulsive interparticle interactions, and therefore as the particle concentration increases, the overall scattering intensity decreases at low q as the two-body interactions become more significant. Therefore, the two-body interactions between sterically stabilized nanocrystals can be determined by measuring the change in the scattered intensity at low angles as a function of concentration for dilute dispersions. For very dilute, weakly interacting dispersions of particles, deviations from the shape factor can be very small. Accurate recovery of $S(q,c)$ for such systems can be complicated, as point-by-point division of $I(q,c)$ by the shape factor can enhance instrument noise, masking the true form of $S(q,c)$. An additional level of bias can also be introduced, as this method requires assumption about the form of the shape factor. For these reasons it is desirable to utilize a method that takes advantage of the measurable deviations in scattering due to changes in intensity (Figure 2), and does not require prior assumptions about the form of the shape factor or the use of very highly concentrated dispersions, and furthermore gives concentration-independent information (i.e., A_2) about the strength of interactions. Using a Zimm analysis based on the relationship

$$\frac{Kc}{I(q,c)} = \frac{1}{M_w P(qR)} + 2A_2c \quad (2)$$

where K is an optical constant based on the electron density of the scatterers and the optics of the system, A_2 can be measured directly from scattering experiments.²⁶

Despite the importance of interparticle interactions between dispersed nanocrystals for understanding and controlling particle deposition, separation, and synthesis, there have been very few quantitative measurements of the interaction potential between organic monolayer-coated nanocrystals. Notable exceptions include osmometry and SAXS measurements of trioctylphos-

phine (TOP)- and trioctylphosphine oxide (TOPO)-coated CdSe nanocrystal dispersions^{30,31} and SAXS measurements of dried silver nanocrystal films.²⁰ To date, we are not aware of any similar studies utilizing alkyl-coated gold nanocrystals. Here we present concentration-dependent small-angle X-ray scattering data measured at low q from dilute dispersions of dodecanethiol-coated gold nanocrystals ranging from 2 to 6 nm diameter. The second virial coefficient is extracted from the data using a modified Zimm analysis and compared to model predictions of the solvent-mediated two-body interaction potential. The values of the virial coefficients indicate that the particles are significantly more attractive than hard spheres. The particle interaction potential calculated from a simple steric stabilization model accounting for van der Waals attraction between metal cores and osmotic repulsion between adsorbed chains also overpredicts the repulsive forces between nanocrystals, in particular for nanocrystals in the small size range that exhibit significantly greater interparticle attraction than expected.

Experimental Section

Gold Nanocrystal Preparation. Dodecanethiol-passivated gold nanocrystals were synthesized using a two-phase arrested precipitation technique.^{32,33} All chemicals were purchased and used as received from Aldrich Chemical Co. An aqueous tetrachloroaurate solution (0.38 g of $\text{HAuCl}_4 \cdot 3\text{H}_2\text{O}$ in 36 mL of deionized water) is combined with an organic solution containing a phase transfer catalyst (2.7 g of $[\text{CH}_3(\text{CH}_2)_7]_4\text{NBr}$ in 25 mL of toluene). The gold ions are transferred into the organic phase during vigorous stirring, after which the aqueous phase is discarded. An aqueous solution containing a reducing agent (0.5 g of NaBH_4 in 30 mL of deionized water) is then added, and the solution is stirred for up to 24 h. Performing the reduction in the presence of 240 μL of dodecanethiol ($\text{C}_{12}\text{H}_{25}\text{SH}$) results in gold nanocrystals with core diameters between approximately 15 and 30 Å. Alternatively, addition of thiol after NaBH_4 addition produces nanocrystals with core diameters of up to approximately 60 Å. The thiol bonds to the gold surfaces, exposing a hydrocarbon layer that provides a steric barrier to further growth or aggregation. The organic phase containing the nanocrystals is finally collected. The particles are then precipitated with ethanol and collected by centrifugation. The supernatant, containing reaction byproducts and excess reactants, is discarded, and the nanocrystals are redispersed into toluene. The nanocrystals obtained at this step are too polydisperse for effective SAXS measurements, as the size distribution broadens the size-dependent oscillations into a meaningless smoothly decaying scattering curve. Therefore, the nanocrystal size distribution must be narrowed by size-selective precipitation for the measurements. The nanocrystals are redispersed in toluene and titrated carefully with ethanol until reaching a barely perceptible opalescence, indicating that the largest particles in the dispersion have begun to precipitate. The dispersion is then centrifuged to isolate the largest particles in the precipitate from the smallest particles that remain suspended in the supernatant.⁶ The alkane layer is chemically stable and provides dispersibility in nonpolar organic solvents and allows the nanocrystals to be reversibly precipitated and redispersed multiple times before significant particle degradation occurs.

Small-Angle X-ray Scattering Measurements. Size-selected fractions of gold nanocrystals were weighed on a microbalance with an accuracy of ± 0.1 mg. The nanocrystals were then redispersed into a measured volume of toluene and carefully diluted, producing a series of dispersions of known mass concentration. The range of concentrations for each set of

dispersions was typically between 1 and 3 mg/mL. All experiments were carried out at 23 ± 0.5 °C. The samples were characterized using small-angle X-ray scattering (SAXS); X-rays were produced from a rotating copper-anode generator (Bruker Nonius) operated at 3.0 kW, and scattered photons were collected on a multiwire gas-filled detector (Molecular Metrology, Inc.). The scattering angle was calibrated using a silver behenate ($\text{CH}_3(\text{CH}_2)_{20}\text{COOAg}$) standard, and all experimental data were corrected for background scattering and sample absorption.

Results

Modified Zimm Method. At zero scattering angle, making use of the fact that $P(qR) = 1$ at $q = 0$, the Zimm equation (eq 2) reduces to

$$\frac{1}{M_w c} = \frac{K}{I(0, c)} - 2A_2 \quad (3)$$

The weight-average molecular weight is readily determined from the average nanocrystal diameter and size distribution determined from the scattering data in the Porod region as described above:

$$M_w = \frac{\sum_R n_R m_R^2}{\sum_R n_R m_R} \quad (4)$$

where n_R and m_R are the number fraction and mass of nanocrystals with radius R , respectively. m_R is calculated using the bulk density of gold. Extrapolating the scattering data to zero scattering angle (i.e., $q = 0$) yields a value for $I(0, c)$. At small values of q the scattered intensity is well approximated by $I(q, c) = I(0, c) \exp(-q^2 R_g^2/3)$, where R_g is the electronic radius of gyration of the nanocrystal and is related to the actual radius by $R_g = R\sqrt{3/5}$.^{23,24,30} Extrapolation of the scattering data to zero scattering angle is then easily accomplished by plotting the data in Guinier form, i.e., $\ln[I(q, c)]$ vs q^2 , and extending the linear portion of the scattering data.

Figure 3 shows $1/M_w c$ plotted against $1/I(0, c)$ for a series of nanocrystal sizes at varying dispersion concentration. The y-intercept of these plots is the osmotic second virial coefficient, A_2 . (Based on the uncertainty in the experimental measurements, the error in the measurement of the second virial coefficient is expected to be less than 30%. Measurements for some of the samples were repeated using the same solutions; the maximum difference in the measurements was 21%, within the expected range of experimental uncertainty.) The measured values of A_2 were the same magnitude to an order of magnitude larger than those recently measured using osmometry for stable, TOPO-capped CdSe nanocrystals in toluene.³¹ The larger values are expected given the Hamaker constant for metals is approximately 2–5 times larger than that of semiconductors similar to CdSe.^{31,34}

SAXS experiments by Mattoussi et al. showed that interactions between poorly capped CdSe nanocrystals can be strongly affected by the amount of free capping ligand in solution.³⁰ For example, scattering in the Guinier region was strongly affected by the addition of excess TOP/TOPO ligands to form a 27 mM solution, indicating a change in the nanocrystal interaction strength. Similar experiments were carried out for the present system: scattering was obtained from several sizes of gold nanocrystals prepared using the experimental procedures re-

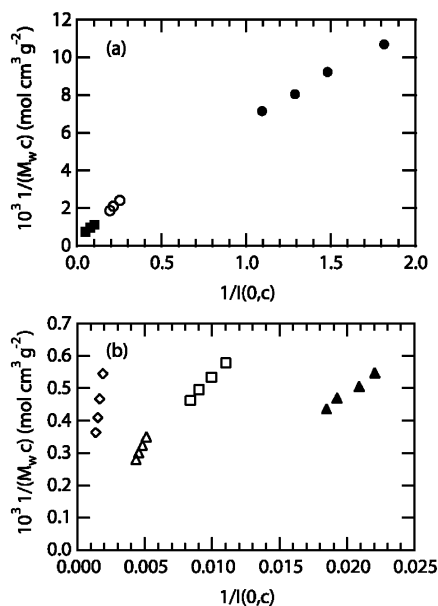


Figure 3. Zimm plot data used to calculate values of the second virial coefficient, A_2 . Because of the range in molecular weights and intensity of the scattering data, the data sets have been separated to avoid overlap of the data points. Data for nanocrystals with average core diameters of 22.0 (●), 30.0 (○), and 37.6 Å (■) are shown in (a). Data for nanocrystals with average core diameters 42.0 (□), 42.8 (▲), 49.0 (△), and 52.6 Å (◇) are shown in (b).

ported above as well as where excess dodecanethiol was added to form a 40 mM solution. As shown in Figure 4, the scattering in the Guinier region was unaffected, indicating that the gold nanocrystals used for the virial coefficient measurements are well-passivated and negligibly affected by the presence of small amounts of excess free ligand in solution. This effect is unlikely to hold for solutions with a high volume fraction of thiol, where the change in the solvation and screening properties of the medium surrounding the nanocrystals would show large deviations from toluene. Scattering data were also obtained from a nanocrystal sample after repeated cycles of precipitation using excess ethanol and redispersed in toluene (Figure 5). Deviations in the scattering curves—indicating changes in interparticle interactions relative to the original sample—were observed only after several washing cycles, indicating that the thiol–gold bond is relatively strong and the nanocrystal dispersion is quite stable.

Second Virial Coefficients. For comparison of the measured osmotic second virial coefficients A_2 with model pair interaction potentials $u(r)$, A_2 must be converted to the statistical second virial coefficient B_2 using eq 1. The important consideration here is that A_2 has units of $\text{cm}^3 \text{ mol/g}^2$, in terms of the *solvent* volume, whereas B_2 has units of cm^3 in terms of *solute* volume. Therefore, the ratio of molar volumes (\bar{V}_i), $v_c = \bar{V}_{\text{solvent}}/\bar{V}_{\text{nanocrystal}} = (M_{w,\text{solvent}}\rho_{\text{solvent}})/[(4\pi/3)(R + \delta)^3 N_A]$, was used to convert the measured values of A_2 to the corresponding values of B_2 . \bar{V}_{solvent} is the molar volume of solvent ($106 \text{ cm}^3/\text{mol}$ for toluene), and δ is the capping ligand length. Figure 6a shows the values of B_2 determined for dodecanethiol-coated Au nanocrystals of varying diameter dispersed in toluene. Nanocrystals larger than approximately 40 Å exhibit overall repulsive interactions between particles, with positive values of B_2 . Particles smaller than 40 Å, on the other hand, exhibit negative values of B_2 , indicating overall attractive interparticle interactions. The 35 Å diameter nanocrystals have the most negative second virial coefficient in this size range. The observed reversal of the interactions, from repulsive to attractive as the nanocrystal size decreases, is consistent with qualitative observations made by

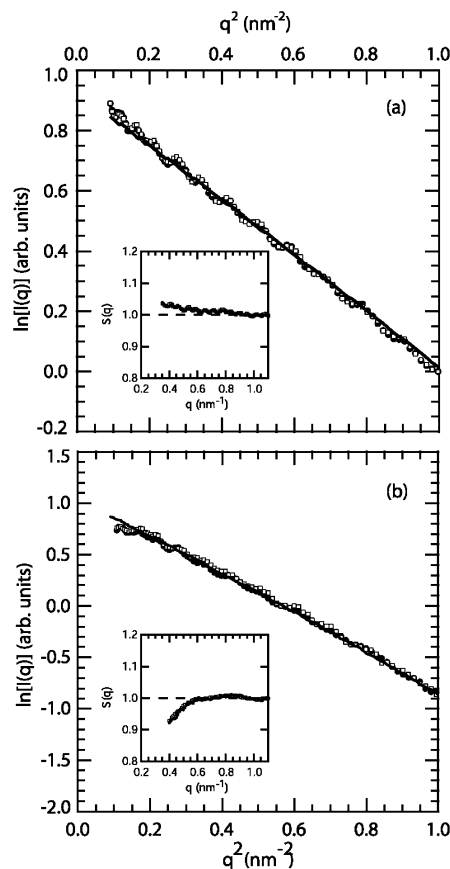


Figure 4. Guinier plots from scattering data obtained for dispersions of (a) 35 and (b) 53 Å gold nanocrystals, at equal concentrations of approximately 3 mg/mL. Each plot shows data for dispersions prepared normally (●) and with excess (40 mM) dodecanethiol ligand added to the solution (□). Despite the large amount of thiol added, the scattering data at low q shows no change, indicating no significant change in interparticle interaction with thiol concentration. For such relatively concentrated dispersions, a measurable structure factor can be recovered from the scattering data and is shown in the inset of each plot.

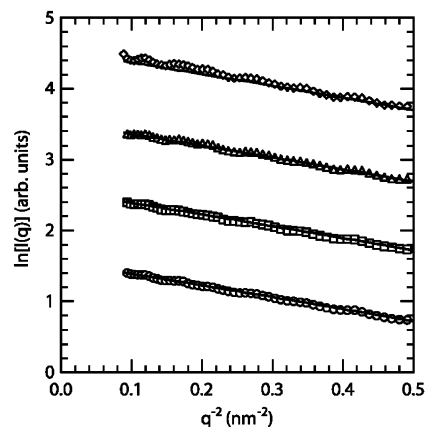


Figure 5. Guinier plots from gold nanocrystal samples which have undergone zero (○), one (□), three (△), and five (◇) washing cycles. The scattering data at low q are unchanged until the fifth washing cycle, which shows attractive interactions due to the removal of excess ligand; further washing cycles result in the irreversible precipitation of nanocrystals from solution.

Mattoussi et al. using SAXS for TOP/TOPO-passivated CdSe nanocrystals.³⁰ Table 1 summarizes the experimental measurements.

The Pair Interaction Potential. The dipole–induced dipole interactions between the metal cores of the nanocrystals give

TABLE 1: Summary of Second Virial Coefficients Determined from SAXS Measurements of Dodecanethiol-Passivated Gold Nanocrystals with Different Core Metal Diameter $2R$, Using a Modified Zimm Analysis

$2R$ (Å)	2σ (Å)	M_w (g/mol) ^a	$A_2 \times 10^5$ (cm ³ mol/g ²)	$B_2 \times 10^4$ (Å ³)
22.0	4.1 (18.6%)	91 000	-82.2	-2.4
30.0	4.8 (16.0%)	234 000	-29.0	-3.7
37.6	4.4 (11.7%)	370 000	-30.0	-6.8
42.0	4.6 (11.0%)	520 000	-5.0	-1.9
42.8	4.5 (10.5%)	547 000	3.4	1.4
49.0	5.7 (11.6%)	840 000	8.6	6.3
52.6	6.5 (12.3%)	1 067 000	8.3	8.7

^a The molecular weight is calculated using eq 4 based on the size distribution of the gold cores.

rise to a strong interparticle attraction that is mediated by the steric layer created by the adsorbed hydrocarbon ligands. The strength of the van der Waals attraction between two spheres of equal radius R depends on the value of the solvent-retarded Hamaker constant A :^{34,35}

$$\Phi_{\text{vdW}}(r) = -\frac{A}{6} \left[\frac{2R^2}{r^2 - 4R^2} + \frac{2R^2}{r^2} + \ln \left(\frac{r^2 - 4R^2}{r^2} \right) \right] \quad (5)$$

There is a significant amount of uncertainty as to the precise value of A ; however, it ranges from 1.1 to 3.1 eV depending on the medium separating the particles,^{22,34} and for simplicity in our calculations we take a value of 3 eV. In a good solvent, the ligand chains extend away from the particle surfaces and fluctuate rapidly. As two particles collide, solvent is pushed out of the intervening space between the particles, thus creating a large osmotic pressure gradient between the ligand layer and the surrounding solvent. Therefore, as a first approximation, the total pair interaction potential $u(r)$ can be approximated as the sum of the van der Waals attraction between the metal cores and the osmotic repulsion between the ligands:³⁶

$$u(r) = \Phi_{\text{vdW}} + \Phi_{\text{osm}} \quad (6)$$

For our calculations of the osmotic repulsion, we make use of the model proposed by Vincent and co-workers that accounts for the capping ligand length δ , the molecular volume of the solvent v_{solv} , the volume fraction of the ligand extending from the nanocrystal surface ϕ , and the Flory–Huggins interaction parameter between the ligand and solvent χ :³⁷

$$\Phi_{\text{osm}}(r) = \frac{4\pi R k_B T}{v_{\text{solv}}} \phi^2 \left(\frac{1}{2} - \chi \right) \left(\delta - \frac{r - 2R}{2} \right)^2, \quad \delta < r - 2R < 2\delta \quad (7a)$$

$$\Phi_{\text{osm}}(r) = \frac{4\pi R k_B T}{v_{\text{solv}}} \phi^2 \left(\frac{1}{2} - \chi \right) \left[\delta^2 \left(\frac{r - 2R}{2\delta} - \frac{1}{4} - \ln \left(\frac{r - 2R}{\delta} \right) \right) \right], \quad r - 2R < \delta \quad (7b)$$

In a good solvent for the ligand, $\chi = 0$. The ligand volume fraction profile ϕ is calculated from the diameter-dependent surface curvature, which is more pronounced in smaller particles, by assuming full ligand extension and using the literature value for the binding density of thiol on gold.^{20,22,36} Model calculations of B_2 using this model (referred to as the osm + vdW model) are shown in Figure 6a and compared to the values measured by SAXS. The osm + vdW model calculations predict $B_2 > 0$ for all particle sizes studied, which is clearly not the case. For the smaller particles, the measured overall interactions between particles are slightly attractive, with $B_2 < 0$.

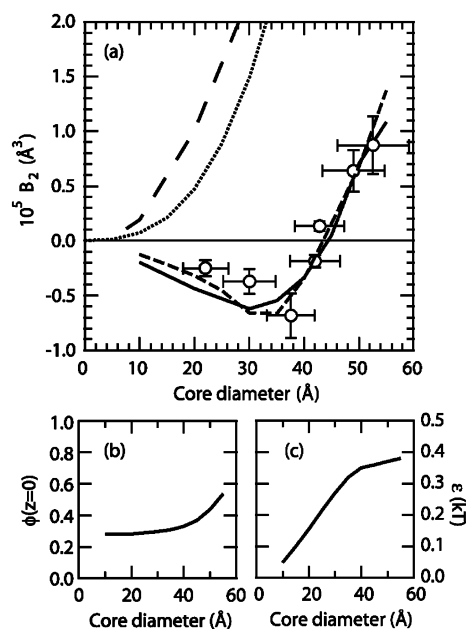


Figure 6. (a) Values of the second virial coefficient determined by SAXS for dodecanethiol-coated gold nanocrystals dispersed in toluene (○). The error bars along the x-axis refer to the standard deviation of the diameter around the mean. The curves correspond to model calculations of B_2 : using a square-well potential for $B_{2,\text{SW}}$ (eq 9) (---), the hard-sphere second virial coefficient for the gold cores $B_{2,\text{HS}}$ (···), and the osm + vdW model discussed above using full thiol coverage (—) and with size-dependent ligand coverage to obtain a best fit to the data (—). (b) The ligand surface coverage as a function of core diameter used to fit the osm + vdW model to the data. (c) The size-dependent magnitude of the well depth used to fit the square-well model to the experimental data; the range of interaction was kept constant at $\alpha = 30$ Å.

To provide a conceptual reference as to how repulsive or attractive the osm + vdW model calculations and measured virial coefficients are, we calculated and plotted the hard-sphere values, $B_{2,\text{HS}} = (2\pi/3)(D_{\text{eff}})^3$, in Figure 6a based on the calculated effective hard-sphere diameter, D_{eff} . The effective hard-sphere diameter takes into account excluded-volume contributions from both the metal core and part of the ligand shell. D_{eff} is taken to be the diameter at which the osmotic repulsion between neighboring particles, calculated using eq 7, reaches $5kT$. The effective hard-sphere diameter was found to increase linearly with the core diameter.

Despite the shallow attractive wells in the interparticle potential predicted by the osm + vdW model (see Figure 7), the excluded-volume effect of the ligands dominates the predicted values of B_2 , consistent with the concept of a “soft-sphere” repulsive interaction potential between particles with an effective hard-sphere diameter greater than the metal core diameter discussed in the literature by Korgel and co-workers.⁷ The positive values of B_2 , which increase with particle diameter, result from the excluded volume of the particles. The fact that the measured values of B_2 are significantly more negative than both $B_{2,\text{HS}}$ and B_2 calculated using the osm + vdW model indicate that the interparticle attraction in a good solvent is more significant than anticipated. These results are in fact consistent with some recent observations of unexpectedly significant interparticle attractions for both silver and gold nanocrystals.^{7,17}

Discussion

To provide a rough gauge as to the extent of interparticle attraction determined from the scattering data, B_2 was calculated

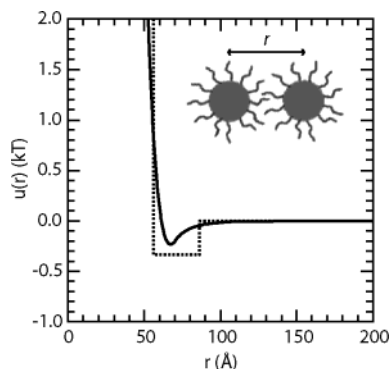


Figure 7. Comparison of the pair potential models described in the text. Shown are the square-well potential (dotted line) and the potential calculated from the van der Waals and osmotic contributions (solid line) for 40 Å nanocrystals. The square-well potential uses the effective hard-sphere diameter, partially taking into account the excluded volume of the ligands. The potentials are plotted as a function of center-to-center distance of the nanocrystals, r , as shown in the inset.

and fit to the data using a square well model for $u(r)$:

$$\frac{u(r)}{kT} = \begin{cases} \infty & r < D_{\text{eff}} \\ -\epsilon & D_{\text{eff}} < r < D_{\text{eff}} + \alpha \\ 0 & r > D_{\text{eff}} + \alpha \end{cases} \quad (8)$$

where α and ϵ are the potential well width and depth, respectively. Although simplistic, the square-well model provides an analytic expression for the second virial coefficient:

$$B_{2,\text{sw}} = \frac{2\pi}{3}(D_{\text{eff}})^3 \left[1 - \left(\frac{(D_{\text{eff}} + \alpha)^3}{(D_{\text{eff}})^3} - 1 \right) (e^{\epsilon/kT} - 1) \right] \quad (9)$$

which can be readily fit to the data to approximate the interparticle interactions. We are mostly interested in determining how much deeper the interaction potential is than the predicted value based on the osm + vdW model. Therefore, taking α to be a representative value of 30 Å and using an effective hard-sphere diameter that includes the ligand excluded volume using the approach described above for calculating $B_{2,\text{HS}}$, the data were fit to eq 9 to determine values of ϵ consistent with the experimental data. The values of ϵ used to fit the experimental data increase with nanocrystal size, from 0.1 kT to 0.4 kT (Figure 6c). Increasing interparticle attraction with increasing particle diameter is consistent with crude expectations based on the size-dependent enhancement in van der Waals attraction. Comparison between the osm + vdW and square-well models is shown in Figure 7 for nanocrystals with a 40 Å diameter core. The repulsive behavior calculated from the osm + vdW model is well-approximated using the effective hard-sphere diameter to calculate the square-well potential. The square-well model, however, predicts a wider and slightly deeper potential well than is calculated using the osm + vdW model.

The deeper attraction between nanocrystals in the square-well model could result from several factors, including a less than closest-packed ligand surface coverage. Although the addition of excess thiol does not change the measured second virial coefficient, and there does not appear to be significant ligand desorption with precipitation and exposure to antisolvent, it is possible that ligand fluctuations prevent a closest-packed thiol layer from forming on the nanocrystal surface. The osm + vdW model can be used to account for the effect of ligand surface coverage on the interaction potential. For straight-chain ligands extending radially from the surface of the nanocrystal,

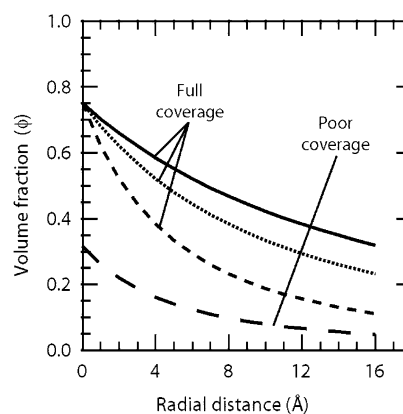


Figure 8. Ligand volume fraction profiles calculated using eq 10 as a function of radial distance from the nanocrystal surface. Calculated profiles are shown for (top to bottom) full surface coverage and nanocrystal core diameters of 60, 40, and 20 Å and for 20 Å particles with poor surface coverage (determined from the fit of the osm + vdW model to the experimental data for the smaller nanocrystals).

the volume fraction ϕ occupied by the ligand around the particle will depend on the radius of curvature and relative surface coverage of the thiol headgroups. The radial dependence of ϕ can be calculated from geometric arguments as^{22,36}

$$\phi(z) = \frac{SA_{\text{thiol}}R}{(R+z)\theta_{\text{thiol}}} \quad (10)$$

where z is the radial distance from the surface of the metal core, SA_{thiol} is the ligand cross-sectional area (14.5 Å²), and θ_{thiol} is the surface area per thiol headgroup (16 Å²/thiol).⁷ As shown in Figure 8, the volume fraction decreases moving away from the particle surface; the decrease is much more pronounced for smaller particles with larger radii of curvature. The ligand density is reduced for smaller nanocrystals as a result of surface curvature, which allows closer surface-to-surface approach between smaller nanocrystals than larger particles. Larger particles, in contrast, experience significant steric repulsion from the more densely packed ligands and the cores are not able to approach as closely. To obtain a fit of modeled B_2 values to the experimental data, calculations using the osm + vdW model were also done in which the ligand surface coverage (i.e., $\phi(z=0)$) was varied as a fitting parameter. Figure 6b shows the values of $\phi(z=0)$ that provided the best fit of the osm + vdW model to the experimental data. The ligand surface coverage ranges from approximately 30% for the small nanocrystals (<40 Å) up to approximately 60% or higher for the nanocrystals in the larger size range (Figure 4b). For comparison, Korgel et al. measured the thiolate surface coverage of silver nanocrystals between 40 and 70 Å and found a value of $75 \pm 10\%$.⁷

Conclusions

Small-angle X-ray scattering data analyzed within the framework of the Zimm method provide a useful, general method for determining interparticle interactions in dilute nanocrystal dispersions. The measured virial coefficients were significantly more negative than expected for purely repulsive potentials, indicating that interparticle attractions can be significant between sterically stabilized nanocrystals in good solvents for the ligands. The attractive energy potential between the particles is nonetheless far smaller than the $3/2kT$ limit that would lead to immediate flocculation. Despite its simplicity, the square-well potential replicated the size-dependent virial coefficients to provide insight into the nature of the interparticle interactions. Using this

potential, the larger particles exhibit larger interparticle attractions, as expected based on consideration of the size-dependent van der Waals attraction between particles. More detailed calculations of the interparticle potential, accounting explicitly for the repulsive stabilization provided by the ligands, suggest that the nanocrystal interactions may be very strongly influenced by the extent of ligand surface coverage on the nanocrystals. Further modeling and experimental work should help to elucidate the role that solvent quality, nanocrystal composition, and other outside forces play in dispersion stabilization of hydrocarbon-coated nanocrystals. A thorough understanding of solvent-mediated interactions should provide a basis for better control of nanoparticle self-assembly and phase behavior.

Acknowledgment. This work is supported in part by the Welch Foundation, the STC Program of the National Science Foundation under Agreement No. CHE-9876674, and the Texas Higher Education Coordinating Board through their ATP program.

References and Notes

- (1) Link, S.; El-Sayed, M. A. *Annu. Rev. Phys. Chem.* **2003**, *54*, 331.
- (2) Shenhar, R.; Rotello, V. M. *Acc. Chem. Res.* **2003**, *36*, 549.
- (3) West, J. L.; Halas, N. J. *Annu. Rev. Biomed. Eng.* **2003**, *5*, 285.
- (4) Compañó, R.; Molenkamp, L.; Paul, D. J. *Technology Roadmap for Nanoelectronics, European Commission Information Society Technologies Programme: Future and Emerging Technologies, Microelectronics Advanced Research Initiative*; <http://nanoworld.org/NanoLibrary/nanoroad.pdf>.
- (5) For example, see: *Semiconductor and Metal Nanocrystals: Synthesis and Electronic and Optical Properties*; Klimov, V. I., Ed.; Marcel Dekker: New York, 2003 and references contained therein.
- (6) Murray, C. B.; Norris, D. J.; Bawendi, M. G. *J. Am. Chem. Soc.* **1993**, *115*, 8706.
- (7) Korgel, B. A.; Fullam, S.; Connolly, S.; Fitzmaurice, D. *J. Phys. Chem. B* **1998**, *102*, 8379.
- (8) Korgel, B. A.; Fitzmaurice, D. *Phys. Rev. Lett.* **1998**, *80*, 3531.
- (9) Connolly, S.; Fullam, S.; Korgel, B. A.; Fitzmaurice, D. *J. Am. Chem. Soc.* **1998**, *120*, 2969.
- (10) Ge, G.; Brus, L. *J. Phys. Chem. B* **2000**, *104*, 9573.
- (11) Ge, G.; Brus, L. E. *Nano Lett.* **2001**, *1*, 219.
- (12) Gray, J. J.; Harley Klein, D.; Bonnacaze, R. T.; Korgel, B. A. *Phys. Rev. Lett.* **2000**, *85*, 4430.
- (13) Gray, J. J.; Klein, D. H.; Korgel, B. A.; Bonnacaze, R. T. *Langmuir* **2001**, *17*, 2317.
- (14) Stowell, C.; Korgel, B. A. *Nano Lett.* **2001**, *1*, 595.
- (15) Lin, X. M.; Jaeger, H. M.; Sorensen, C. M.; Klabunde, K. J. *J. Phys. Chem. B* **2001**, *105*, 3353.
- (16) Moriarty, P.; Taylor, M. D. R.; Brust, M. *Phys. Rev. Lett.* **2002**, *89*, 248303/1.
- (17) Sigman, M. B., Jr.; Saunders, A. E.; Korgel, B. A. *Langmuir*, **2004**, *20*, 978–983.
- (18) Rabani, E.; Reichman, D. R.; Geissler, P. L.; Brus, L. E. *Nature (London)* **2003**, *426*, 271.
- (19) Shah, P. S.; Novick, B. J.; Hwang, H. S.; Lim, K. T.; Carbonell, R. G.; Johnston, K. P.; Korgel, B. A. *Nano Lett.* **2003**, *3*, 1671.
- (20) Korgel, B. A.; Fitzmaurice, D. *Phys. Rev. B* **1999**, *59*, 14191.
- (21) Whetten, R. L.; Shafigullin, M. N.; Khoury, J. T.; Schaaff, T. G.; Vezmar, I.; Alvarez, M. M.; Wilkinson, A. *Acc. Chem. Res.* **1999**, *32*, 397.
- (22) Shah, P. S.; Holmes, J. D.; Johnston, K. P.; Korgel, B. A. *J. Phys. Chem. B* **2002**, *106*, 2545.
- (23) *Small-Angle X-ray Scattering*; Glatter, O., Kratky, O., Eds.; Academic Press: New York, 1982.
- (24) Guinier, A.; Fournet, G. *Small-Angle Scattering of X-Rays*; Wiley: New York, 1955.
- (25) Here, the term “noninteracting” generally refers to the fact that the scattered X-rays from each sphere do not interfere with X-rays scattered from other spheres; therefore, the total angle-dependent scattering is simply the sum of X-rays scattered from each individual in the ensemble. These conditions hold when the dispersion is dilute—so the scattered X-ray “density” is low—and when particles do not interact or stick to an appreciable amount.
- (26) Zimm, B. H. *J. Chem. Phys.* **1948**, *16*, 1093.
- (27) In Zimm’s analysis,²⁶ he actually found that $S(q) = (1 - \xi P(qR))/(1 + \xi P(qR))^2$ is a better model for extracting the second virial coefficient at higher concentrations, which follows from the well-known Zimm equation, $[Kc/I] = [1/MP(qR)] + 2A_2C$.
- (28) Zamora, P. C.; Zukoski, C. F. *Langmuir* **1996**, *12*, 3541.
- (29) Davis, H. T. *Statistical Mechanics of Phases, Interfaces and Thin Films*; VCH Publishers: New York, 1995.
- (30) Mattoussi, H.; Cumming, A. W.; Murray, C. B.; Bawendi, M. G.; Ober, R. *Phys. Rev. B* **1998**, *58*, 7850.
- (31) Striolo, A.; Ward, J.; Prausnitz, J. M.; Parak, W. J.; Zanchet, D.; Gerion, D.; Milliron, D.; Alivisatos, A. P. *J. Phys. Chem. B* **2002**, *106*, 5500.
- (32) Brust, M.; Walker, M.; Bethell, D.; Schiffrin, D. J.; Whyman, R. *J. Chem. Soc., Chem. Commun.* **1994**, 801.
- (33) Saunders, A. E.; Sigman, M. B., Jr.; Korgel, B. A. *J. Phys. Chem. B* **2004**, *108*, 193.
- (34) Israelachvili, J. *Intermolecular & Surface Forces*, 2nd ed.; Academic Press: San Diego, 1992.
- (35) Hamaker, H. C. *Physica (The Hague)* **1937**, *4*, 1058.
- (36) Shah, P. S.; Husain, S.; Johnston, K. P.; Korgel, B. A. *J. Phys. Chem. B* **2002**, *106*, 12178.
- (37) Vincent, B.; Edwards, J.; Emmett, S.; Jones, A. *Colloids Surf.* **1986**, *18*, 261.